ARCHIVES OF TRANSPORT *ISSN (print):* *0866-9546*
Volume 44, Issue 4, 2017 ***e-ISSN (online):*** *2300-8830*
DOI: *10.5604/01.3001.0010.6164*

DESIGN OF LARGE-SCALE STREAMLINED HEAD CARS OF HIGH-SPEED TRAINS AND AERODYNAMIC DRAG CALCULATION

Zhenfeng Wu[1], Enyu Yang[2], Wangcai Ding[3]

[1,2,3] School of Mechanical and Electrical Engineering, Lanzhou Jiaotong University, Lanzhou, China

[1]e-mail: wzhf@mail.lzjtu.cn

Abstract: *Aerodynamic drag plays an important role in high-speed trains, and how to reduce the aerodynamic drag is one of the most important research subjects related to modern railway systems. This paper investigates a design method for large-scale streamlined head cars of high-speed trains by adopting NURBS theory according to the outer surface characteristics of trains. This method first created the main control lines of the driver cab by inputting control point coordinates; then, auxiliary control lines were added to the main ones. Finally, the reticular region formed by the main control lines and auxiliary ones were filled. The head car was assembled with the driver cab and sightseeing car in a virtual environment. The numerical simulation of train flow field was completed through definition of geometric models, boundary conditions, and space discretization. The calculation results show that the aerodynamic drag of the high-speed train with large-scale streamlined head car decreases by approximately 49.3% within the 50-300 km/h speed range compared with that of the quasi-streamlined high-speed train. This study reveals that the high-speed train with large-scale streamlined head car could achieve the purpose of reducing running aerodynamic drag and saving energy, and aims to provide technical support for the subsequent process design and production control of high-speed train head cars.*

Key words: *high speed train, streamlined head car, NURBS, numerical simulation, aerodynamic drag.*

1. Introduction

The high speed railway has become an inexorable trend of the rail transit because it is not only faster, safer and more comfortable, but also can reduce environmental pollution (Paz et al., 2015; Lee et al., 2016).

The high-speed trains, a key subsystem of the high speed railway, have became an important symbol of the high-tech development of country. The problem of aerodynamic drag which is proportional to the square of the speed of train becomes more and more important with the increase of train speed. Some research has indicated that the aerodynamic drag in the proportion of total drag could reach over 70% when train speed reaches more than 200 km/h (Watkins et al., 1992; Baker, 2010). Since the power of train is proportional to the cube of the train speed, it's necessary to minimize the aerodynamic drag for the sake of energy saving.

There are many parts which have obvious effect on the aerodynamic drag of the train such as the head car, pantograph, apron board, outer vestibule diaphragm and so on, especially the shape of the head car which has a larger effect on the aerodynamic drag. Up to now, many efforts have been made towards the relationship between the train head type and its aerodynamic drag. Wang et al. (2007) calculated the aerodynamic drag coefficient of high speed train with the Fluent software, and the calculation results were well consistent with the experiment results, which proved the feasibility of simulating the train aerodynamic drag by using the method of CFD (Computational Fluid Dynamics). Tian (2009) divided the aerodynamic drag on the travelling train into pressure drag and friction drag, and researched the causes. The result turned out that the most effective measure to reduce the aerodynamic drag of high speed train was to adopt the streamlined head car. Ku et al. (2010) presented the two-stage optimization design process of train nose shape according to the aerodynamic drag and the micro-pressure wave. They optimized the nose of the head car for the reduction of the micro-pressure wave in the first stage and then, in the second stage, the 3D nose shape of the head car was optimized to reduce the aerodynamic drag. Minho et al. (2013) optimized the 3D nose shape of head car and the tail car by

adopting CFD method and vehicle modelling function. Their research indicated that the total aerodynamic drag of the optimum shape for the entire train was reduced by 23.0% compared with the total aerodynamic drag of train which only optimized the shape of head car. Zhang et al. (2013) carried out the wind tunnel experiments on the trains with different streamlined shapes. The results showed that the aerodynamic drag can be reduced on condition that the train was equipped with the smoother streamlined head car and sharper nose.

In the previous studies, the objects of the research were almost the head cars of whose streamlined length is less than 10 meters. The documents of research on the aerodynamic performance of the large-scale streamlined head car (its streamlined length is longer than 10 meters) are relatively few. This paper completed the 3D digital design of the large-scale streamlined head car by using the NURBS (Non-Uniform Rational B-Spline) method, and then calculated the aerodynamic drag of the large-scale streamlined train and the quasi-streamlined one with the CFD method respectively.

The paper is organized as follows: the introduction to NURBS method is given in Section 2. Section 3 presents the design process of the large-scale streamlined leading car of high speed train. The calculation process of aerodynamic drag of two types of trains is discussed in Section 4. Section 5 is the conclusion of this paper.

2. Introduction to NURBS Method

Catmull (1978) proposed the concept of NURBS based on the B-spline method. The NURBS method inherits many properties of the non-rational B-spline method, such as local support, convex hull, and invariance under standard geometric transformations. The NURBS method introduces the concepts of control points and weighted factors (Abbas et al., 2014). It does not affect other parts when adjusting local shape of curve or surface by modifying local control points and weighted factors, thereby providing convenience in designing complex surfaces; thus, it is one of the most successful and popular methods used in computer-aided design. The NURBS method can precisely express elementary curve (surface), quadratic curve (surface), and free-form curve (surface) because it offers a common mathematical framework for implicit and parametric polynomial forms (Ibrahim et al., 2011; Gatilov, 2016; Akhras et al., 2016).

2.1. Expression of NURBS Curve

A NURBS curve is a combination of a set of piecewise rational functions with n+1 control points d_i $(i = 0,1,\cdots n)$ and associated weighted factors w_i, which are expressed as follows:

$$C(u) = \frac{\sum_{i=0}^{n} w_i \, d_i \, B_{i,k}(u)}{\sum_{i=0}^{n} w_i \, B_{i,k}(u)} \tag{1}$$

where u is the parametric variable and $B_{i,k}(u)$ represents B-spline basis functions. The control points d_i $(i = 0,1,\cdots n)$ are usually not on the curve, but the shape of the NURBS curve is determined by the control polygon formed by control points. The weighted factors w_i are equivalent to the "gravity" of the control point d_i, i.e., the greater the value is, the closer the control points approach the curve (Tobias et al., 2012). A NURBS curve has $n+k+1$ knots t_i in non-decreasing sequence $t_0 \le t_1 \cdots \le t_{n+k}$ based on the assumption that its basis function is $k-1$ order. The basis function can be written recursively as follows:

$$B_{i,1}(u) = \begin{cases} 1 & for \ t_i \le u < t_{i+1} \\ 0 & otherwise \end{cases} \tag{2}$$

$$B_{i,k}(u) = \frac{u - u_i}{u_{i+k} - u_i} B_{i,k-1}(u) + \frac{u_{i+k+1} - u}{u_{i+k+1} - u_{i+1}} B_{i+1,k-1}(u) \tag{3}$$

2.2. Expression of NURBS Surface

A NURBS surface is defined with parametric variables u and v as follows:

$$S(u,v) = \frac{\sum_{i=0}^{m} \sum_{j=0}^{n} w_{i,j} \, d_{i,j} \, B_{i,k}(u) \, B_{j,l}(v)}{\sum_{i=0}^{m} \sum_{j=0}^{n} w_{i,j} \, B_{i,k}(u) \, B_{j,l}(v)} \tag{4}$$

A NURBS surface has $(m+1)(n+1)$ control points $d_{i,j}$ and weighted factors $w_{i,j}$, which have the effect of stretching and compressing to a point on the NURBS surface. The number of NURBS surface knots is $(m+k+1)(n+l+1)$ based on the assumption that the order of basis functions along the two parametric axes is $k-1$ and $l-1$. The non-decreasing knot sequence is $t_0 \le t_1 \cdots \le t_{m+k}$ along the u axis and $s_0 \le s_1 \cdots \le s_{m+k}$ along the v axis, respectively, and the parametric domain is $t_{k-1} \le u \le t_{m+l}$ and $s_{l-1} \le v \le s_{n+l}$. The basis function $B_{i,k}(u)$ is completely the same as formulas (2)–(3) and $B_{j,l}(v)$ is defined as follows:

$$B_{j,l}(v) = \frac{v - v_j}{v_{j+l} - v_j} B_{j,l-1}(v) + \frac{v_{j+l+1} - v}{v_{j+l+1} - v_{j+1}} B_{j+1,l-1}(v) \quad (5)$$

3. Design process of head cars

To reduce the aerodynamic drag and strength of micro-pressure wave effectively when a train is running at high speed, the head car of the train should be designed with a streamlined shape (Moon et al., 2014). In this study, the length of the head car is assumed to be more than 10 meters. For design convenience, the head car could be divided into two parts, namely, driver cab and sightseeing car, and then assembled in a virtual environment. Owing to the high-degree symmetry of the driver cab, only half of the driver cab needs to be designed in longitudinal direction to achieve the complete model by symmetry operation.

3.1. Main control lines of driver cabs

The main control lines of the driver cab include maximum overlooking control line, maximum longitudinal symmetry control line, cross-sectional contour lines, and adjustable lines. We have to input 3D coordinates of control points d_i ($i = 0,1,\cdots n$) of the aforementioned control lines continuously. The half digital model of the driver cab is formed by 22 control lines, which amount to a total of 215 control points. Besides, all the main control lines should be faired, and the maximum deviation value should not exceed 0.001 mm. The finished half digital model of the driver cab is shown in Fig. 1.

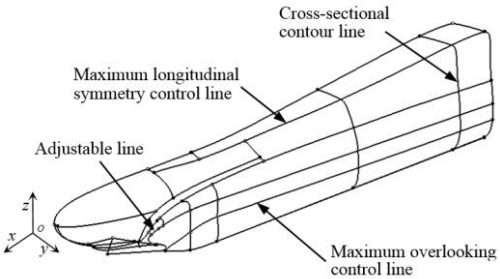

Fig. 1. Main control lines of the driver cab

3.2. Auxiliary control lines of driver cabs

The main lines cannot be used to create the driver cab surface directly because of their larger spacing. Thus, some auxiliary control lines need to be created appropriately. The method of creating the auxiliary control lines first involves arraying the yz plane by unequal distance. The determining principle of distance is that it can be larger if the surface shape of an area changes slightly and smaller if the surface shape of an area changes significantly. The arrayed planes intersect with the main control lines into a series of intersections that could be linked by the NURBS curve. The auxiliary control lines in the xz plane direction are completed through the same steps as those in the yz direction. The spatial network structure of the driver cab is formed by the main control lines and auxiliary ones shown in Fig. 2.

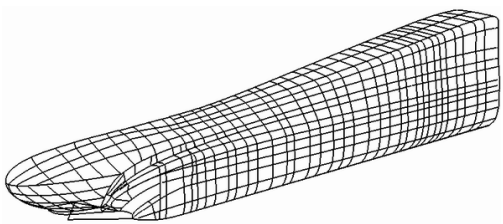

Fig. 2. Control lines of the driver cab

After the previous steps, the NURBS method can be adopted to create the surface of the driver cab. First, all the control lines, including main control and auxiliary control ones, should be broken at the intersections, thereby forming plenty of spatial grids

that are independent from each other, and then filling all the grids to generate small pieces of the NURBS surface. To ensure that the entire surface of the driver cab is smooth, all the NURBS surfaces must be at a tangent. The final driver cab model is completed by symmetry operation of the half model in longitudinal direction, and the front window, side doors, and headlight are created by incision and combination operation. The finished digital surface model of the driver cab is shown in Fig. 3.

Fig. 3. Surface model of the driver cab

3.3. Virtual assembly of head cars

Numerous studies have shown that the best cross-section shape of a sightseeing car is that of a drum, which ensures that the train would have good aerodynamic performance (Gilbert et al., 2013; Lucanin et al., 2012). A 2D sketch of the sightseeing car cross-section, which has a total area of 11.3 m^2, is shown in Fig. 4. In this figure, the outer shape of the sightseeing car is stretched and the side windows are created by segmentation operation.

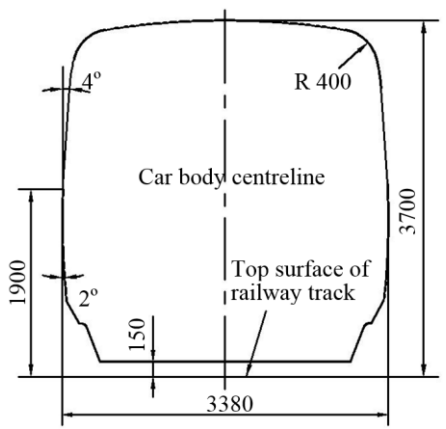

Fig. 4. Cross-Section of the sightseeing car (unit:mm)

The head car is assembled with the driver cab and the sightseeing car through the steps of surface adaption and alignment in a virtual environment. In this study, the head car is rendered for improved visual aesthetics, as shown in Fig. 5. The basic dimensions of the head car are listed in Table 1.

Fig. 5. Surface model of the head car

Table 1. Basic dimensions of the head car

Position	Length [m]	Width [m]	Height [m]
Driver cab	14.40	3.38	3.7
Sightseeing car	11.60	3.38	3.7
Head car	26.00	3.38	3.7

4. Numerical simulation of aerodynamic drag between two types of train

At present, a certain number of quasi-streamlined high-speed trains with shorter driver cabs are used in China (Yao et al., 2012). One type of head car of quasi-streamlined high-speed train is shown in Fig. 6.

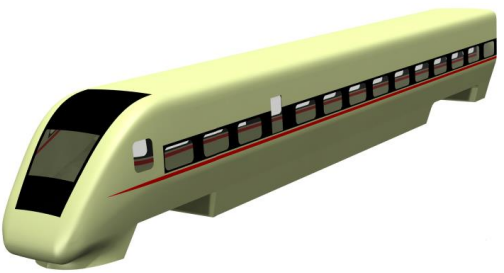

Fig. 6. Heading car of the type A train

To facilitate subsequent calculation and explanation, we name the train with quasi-streamlined head car type A train, and the train with large-scale streamlined head car type B train. The CFD method is a widely used technology for determining the

aerodynamic drag of trains in flow field. Compared with traditional experiments such as wind tunnel and dynamic model experiments, calculating the aerodynamic drag by using the CFD method could save costs and shorten the design cycle (Herbst et al., 2014). In this study, the aerodynamic drag calculation is conducted using Ansys Fluent 12.0 software.

4.1. Control Equations

The effect to the flow field caused by air density can be ignored in cases when the train is running in open air. Thus, we adopt standard $k-\varepsilon$ turbulence model to describe the flow field, and the relevant control equations can be defined as follows (Oh et al., 2016):

$$\frac{\partial u_i}{\partial x_i} = 0 \tag{6}$$

$$\rho u_j \frac{\partial u_i}{\partial x_j} = -\frac{\partial p}{\partial x_i} + \frac{\partial}{\partial x_j}\left[(\mu+\mu_t)\left(\frac{\partial u_i}{\partial x_j}+\frac{\partial u_j}{\partial x_i}\right)\right] \tag{7}$$

$$\frac{\partial(\rho k u_i)}{\partial x_i} = \frac{\partial}{\partial x_j}\left[\left(\mu+\frac{\mu_t}{\sigma_k}\right)\frac{\partial k}{\partial x_j}\right] + \mu_t \frac{\partial u_j}{\partial x_i}\left(\frac{\partial u_j}{\partial x_i}+\frac{\partial u_i}{\partial x_j}\right) - \rho\varepsilon \tag{8}$$

$$\frac{\partial(\rho \varepsilon u_i)}{\partial x_i} = \frac{\partial}{\partial x_j}\left[\left(\mu+\frac{\mu_t}{\sigma_\varepsilon}\right)\frac{\partial \varepsilon}{\partial x_j}\right] + C_1 \mu_t \frac{\varepsilon}{k}\frac{\partial u_j}{\partial x_i}\left(\frac{\partial u_j}{\partial x_i}+\frac{\partial u_i}{\partial x_j}\right) - C_2 \rho \frac{\varepsilon^2}{k} \tag{9}$$

In equations (6)–(9), u_i, u_j represent the speed of flow field passing the train; x_i, x_j represent the coordinate component, ρ and p represent the density and pressure of air, respectively; μ represents the dynamic viscosity coefficient of air; μ_t represents the viscosity coefficient of turbulence and $\mu_t = C_\mu \rho k^2 / \varepsilon$; k represents the turbulent kinetic energy; ε represents the dissipation rate of turbulence; and C_μ represents the turbulence constant. In this study, the empirical coefficients of the models are C_u=0.09, C_1=1.44, C_2=1.92, σ_k=1.0, σ_ε=1.3. The cell-centered finite volume method was used to discretize the governing equations (6)–(9), the SIMPLE（Semi-Implicit Method for Pressure Linked Equation） algorithm was employed to decouple the velocity and pressure, the second-order upwind scheme was used to discretize the convection term, and the central difference scheme was used to discretize the dissipation term.

4.2. Dimensions and Grids of Flow Field

The geometric model is assembled with three cars, namely, head, middle, and tail. The head and tail cars have the same length L_1=L_3=26.0 m, and the length of the middle car L_2 is 26.5 m. Thus, the entire length of the geometric model is L=L_1+L_2+L_3=26.0+26.5+26.0=78.5 m. The cars are connected by an outer vestibule diaphragm, and the train geometric model is shown in Fig. 7(a)–(b).

Based on previous calculation experience of wheel-rail trains, the dimensions of flow field could be determined by the total train length L, the inlet direction and width direction 1L, and the outflow direction and height direction 2L (Sun et al., 2016). The overall and local grids of the type B train are shown in Fig. 8(a)–(b).

To simplify the computation and improve the convergence speed, unstructured grids are adopted in the calculating domain, the grids near the train are refined, and the remaining regions are kept sparse. The geometric model dimensions and total number of grids of the two types of train are listed in Table 2.

Table 2. Geometric model dimensions of the two types of train

Train type	Length [m]			Grids [million]
	Head car	Middle car	Geometric model	
A	26.00	26.5	78.5	227.8
B	26.00	26.5	78.5	231.5

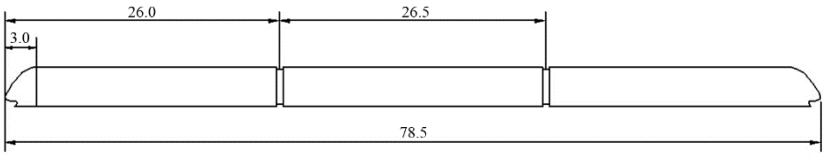

(a) Type A train

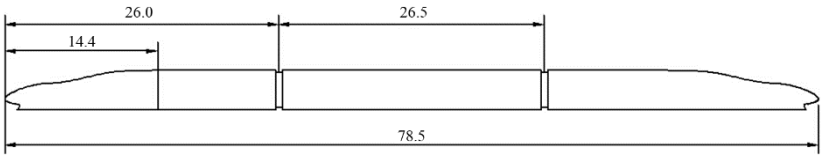

(b) Type B train

Fig. 7. Geometric models of the type A and the type B train（unit:m）

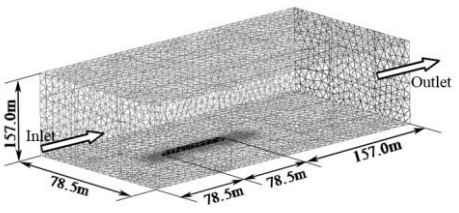

(a) Overall grids

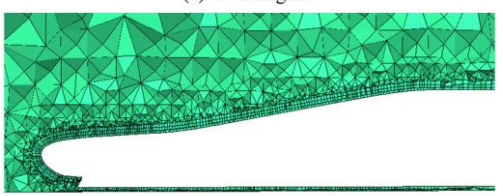

(b) Local grids

Fig. 8. Calculating domain grids of the type B train

4.3. Boundary Conditions

The boundary conditions of the calculating domain are set as follows: speeds of 50, 100, 150, 200, 250, and 300 km/h are set on the inlet section. The hydrostatic of the outlet is set to the standard atmospheric pressure. The top side, both sides of the calculating domain, and the train outer surface are set to no-slip wall boundaries. The train is assumed to be stationary and air is assumed to be flowing during the simulation process. However, in fact, the air and ground are relatively static, and no boundary layer of the air exists at the bottom when the train is running. To simulate the real status of the train, we eliminate the effect of the boundary layer. Furthermore, the bottom surface of the flow field is set to moving wall boundary condition, and its speed is the same as the inflow velocity. The thickness of the boundary layer is set to 3 mm (Jeong et al., 2015).

4.4. Calculation of Surface Pressure

Adopting the aforementioned marshaling form, control equations, flow field, and boundary conditions, we set the inlet speed of the two types of trains to 200 km/h. The surface pressure contour and air trajectories of the head car of two types of trains are calculated and presented in Fig. 9(a)–(b).

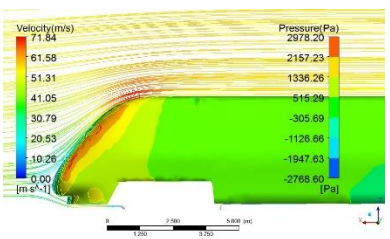

(a) Type A train

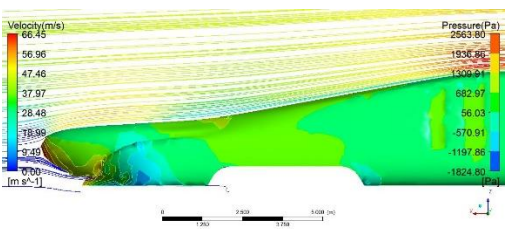

(b) Type B train

Fig. 9. Comparison in surface pressure contour and air trajectories

Fig. 9 shows that the maximum velocity of the air both appears in the positions where the shapes of the head car mutate, i.e., the binding position of the head car and the sightseeing car. The maximum velocity of type A is 71.84 m/s and that of type B is 66.45 m/s. The maximum pressures on the body surface of the two types of trains both appear at the tip of the head cars; the pressure of type A is 2978.2 Pa and that of type B is 2563.8 Pa. The calculation results indicate that type B is better than A in improving the air flow status.

4.5. Calculation of Aerodynamic Drag

To evaluate the aerodynamic performance of two types of trains comprehensively, we set the inlet speed of the two types of trains to 50, 100, 150, 200, 250, and 300 km/h. The aerodynamic drag of the running train is usually classified into differential pressure, frictional, and interference drag. The differential pressure drag is due to the positive pressure near the head car and the negative pressure near the tail car, and the differential pressure drag is affected significantly by the shape of the head and tail cars. The frictional drag is a type of shear force caused by air viscosity and acting on the train body surface, which is related to the train length. The interference drag is due to prominent parts or depressions on the surface of the train such as headlight, armrest, bogie, pantograph, and so on.

Considering that the two types of trains can be equipped with the same bogie and pantograph, we can ignore the interference drag and calculate only the differential pressure and frictional drags. The aerodynamic drag of trains at different speeds is listed in Table 3.

To illustrate the total aerodynamic drag at different speeds of the two types of train intuitively, the speed-aerodynamic drag-fitting curves of the two types of train are shown in Fig. 10.

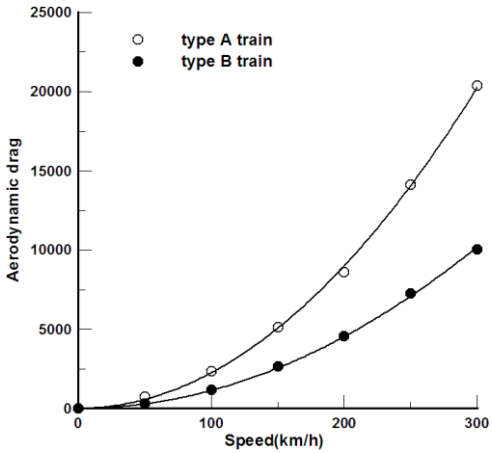

Fig. 10. Speed-Aerodynamic drag-fitting curves of the type A and the type B train

Table 3. Calculating results of the aerodynamic drag of the type A and the type B train at different speeds

Speed [km/h]	Train type	Differential pressure drag [N]	Frictional drag [N]	Total aerodynamic drag [N]	Reduction rate [%]
50	A	560.0	203.7	763.7	59.2
	B	233.1	78.3	311.4	
100	A	1728.5	622.1	2350.6	49.6
	B	831.9	353.0	1184.9	
150	A	3864.6	1283.4	5148.0	48.3
	B	1862.1	798.4	2660.5	
200	A	6744.1	1850.4	8594.5	46.6
	B	2834.0	1751.4	4585.4	
250	A	10761.1	3350.1	14111.2	48.6
	B	4581.6	2668.5	7250.1	
300	A	15532.1	4849.0	20381.1	50.7
	B	6293.4	3750.5	10043.9	

*reduction rate= (total aerodynamic drag of type A train-total aerodynamic drag of type B train)/ total aerodynamic drag of type A train×100%

As shown in Fig. 10, the speed-aerodynamic drag-fitting curves of the two types of train are both quadratic parabola, namely, the total aerodynamic drag is proportional to the square of the train speed. The total aerodynamic drag of the type B train decreases by 59.2% at the speed of 50 km/h, 49.6% at 100 km/h, 48.3% at 150 km/h, 46.6% at 200 km/h, 48.6% at 250 km/h, and 50.7% at 300 km/h compared with that of the type A train. The aerodynamic drag coefficient of a train can usually be expressed as follows:

$$F = C v^2 \tag{10}$$

In formula 10, F is the aerodynamic drag of the train, C is the aerodynamic drag coefficient, and v is the train speed. We obtain the result that $C_A = 0.225$ and $C_B = 0.113$ by fitting the curves in Fig. 10, thereby indicating that the aerodynamic drag coefficient of the type B train is considerably lower than that of the type A train.

The average aerodynamic drag reduction rate of 50–300 km/h can be expressed as follows:

$$r = \frac{\int F_{\mathrm{A}}(v) - \int F_{\mathrm{B}}(v)}{\int F_{\mathrm{A}}(v)} \times 100\,\% \tag{11}$$

In formula 11, $F_{\mathrm{A}}(v)$ is the fitting function of the aerodynamic drag of the type A train, $F_{\mathrm{B}}(v)$ is the fitting function of the aerodynamic drag of the type B train, $F_{\mathrm{A}}(v)$ and $F_{\mathrm{B}}(v)$ are both the functions of the independent variable v. It is concluded from calculation that $r = 49.3\%$.

5. Conclusion

In this study, the design process of the head car outer surface of a large-scale streamlined high-speed train is completed by the NURBS method. Close attention should be paid to the trend and smoothness of the main control lines because these factors directly determine the smoothness of the auxiliary control lines and forming surface.

The calculating results of the flow field indicate that the total aerodynamic drag of the large-scale streamlined high-speed train is obviously decreased compared with that of the quasi-streamlined one within the 50–300 km/h speed range. Thus, applying the large-scale streamlined train, which also represents a future development direction for the head type of railway vehicles, is good for saving energy and improving transport efficiency.

The design model of the large-scale streamlined head car is an important technical reference for the subsequent manufacturing of outer skin plates and frame installation. At the same time, the design program is advisable as long as it can reduce the aerodynamic drag significantly even if it requires decreasing the number of seats in the sightseeing car.

Acknowledgements

The work of this paper is supported by the National Natural Science Foundation of China (Grant No. 11462011) and Project of the Education Department of Gansu Province (No. 2016A-021).

References

[1] ABBAS, M., RAMLI, N., MAJID, A. A., 2014. The representation of circular arc by using rational cubic timmer curve. *Mathematical Problems in Engineering*, 2014, Article ID 408492, 6 pages.

[2] AKHRAS, H. A., ELGUEDJA, T., GRAVOUILA, A., 2016. Isogeometric analysis-suitable trivariate NURBS models from standard B-Rep models. *Science Direct*, 307, pp. 256-274.

[3] BAKER, C., 2010. The flow around high speed trains. *Journal of Wind Engineering and Industrial Aerodynamics*, 98(6/7), pp. 277−298.

[4] CATMULL, E., CLARK, J., 1978. Recursively generated B-spline surfaces on arbitrary topological meshes. *Computer Aided Geometric Design*, 16(6), pp. 350-355.

[5] GATILOV, S. Y., 2016. Vectorizing NURBS surface evaluation with basis functions in power basis. *Computer-Aided Design*, 73, pp. 26-35.

[6] GILBERT, T., BAKER, C., QUINN, A., 2013. Aerodynamic pressures around high-speed trains: the transition from unconfined to enclosed spaces. *Proceedings of the Institution of Mechanical Engineers (Part F: Journal of Rail and Rapid Transit)*, 227(6), pp. 609-622.

[7] HERBST, A. H., MULD, T. W., EFRAIMSSON, G., 2014. Aerodynamic prediction tools for high-speed trains. *International Journal of Rail Transportation*, 2(1), pp. 50-58.

[8] IBRAHIM, T., BAHATTIN, K., 2011. Multi-directional blending for heterogeneous objects. *Computer Aided Design*, 43(8), pp. 863-875.

[9] JEONG, S. M., LEE, S. A., RHO, J. H., et al., 2015. Research of high-speed train pantograph shape design for noise and drag reduction through computational analysis. *Journal of Fluids Engineering*, 20(2), pp. 67-72.

[10] KU, Y. C., KWAK, M. H., PARK, H. I., 2010. Multi-objective optimization of high-speed train nose shape using the vehicle modelling function. In: *48th AIAA Aerospace Science Meeting Including the New Horizons Forum and Aerospace Exposition*, January 2010, Orlando, Fl, USA.

[11] LEE, Y., KIM, K. H., RHO, J. H., et al., 2016. Investigation on aerodynamic drag of Korean high speed train (HEMU-430X) due to roof apparatus for electrical device. *Journal of Mechanical Science and Technology*, 30(4), pp. 1611-1616.

[12] LUCANIN, VOJKAN, J., MIRJANA, A., 2012. Determining the influence of an air wave caused by a passing train on the passengers standing at the platform. *International Journal of Heavy Vehicle Systems*, 19(3), pp. 299-313.

[13] MINHO, K., SUHWAN, Y., YEONGBIN, L., 2013. Optimum nose shape of a front-rear symmetric train for the reduction of the total aerodynamic drag. *Journal of Mechanical Science and Technology*, 27(12), pp. 3733-3743.

[14] MOON, J. S., KIM, S. W., KWON, H. B., 2014. A study on the aerodynamic drag reduction of high-speed train using bogie side fairing. *Journal of Fluids Engineering*, 19(1), pp. 41-46.

[15] OH, H. K., KWON, H., KWAK, M., et al., 2016. Measurement and analysis for the upper side flow boundary layer of a high speed train using wind tunnel experiments with a scaled model. *Journal of the Korean Society for Railway*, 19(1), pp. 11-19.

[16] PAZ, C., SUÁREZ, E., GIL, C., et al., 2015. Numerical study of the impact of windblown sand particles on a high-speed train. *Journal of Wind Engineering and Industrial Aerodynamics*, 145, pp. 87-93.

[17] SUN, B., GAO, S., MA CH., 2016. Mathematical methods applied to economy optimization of an electric vehicle with distributed power train system. *Mathematical Problems in Engineering*, 2016, Article ID 4949561, 14 pages.

[18] TIAN, H. Q., 2009. Formation mechanism of aerodynamic drag of high-speed train and some reduction measures. *Journal of Central South University of Technology*, 16(1), pp. 166-171.

[19] TOBIAS, M., ELAINE, C., ROBERT, M., 2012. Mixed-element volume completion from NURBS surfaces. *Computers & Graphics*, 36(5), pp. 548-554.

[20] WANG, D. P., ZHAO, W. ZH., MA, S. Q., 2007. Application of CFD numerical simulation in high speed train design. *Journal of the China Railway Society*, 29(5), pp. 64-68.

[21] WATKINS, S., SAUNDERS, J., KUMAR, H., 1992. Aerodynamic drag reduction of goods trains. *Journal of Wind Engineering and Industrial Aerodynamics*, 40(1), pp. 147-178.

[22] YAO, SH. B., GUO, D. L., YANG, G. W., 2012. Three-dimensional aerodynamic optimization design of high-speed train nose based on GA-GRNN. *Science China (technology science)*, 55(11), pp. 3118-3130.

[23] ZHANG, Z. ZH., ZHOU, D., 2013. Wind tunnel experiment on aerodynamic characteristic of streamline head of high speed train with different head shapes. *Journal of Central South University (Science and Technology)*, 44(6), pp. 2603-2608.